Effect of vertical electromagnetic stirring on solute distribution in billet continuous casting process

Tao Wang, En-Gang Wang, Yves Delannoy, Yves Fautrelle, Olga Budenkova

Effect of vertical electromagnetic stirring on solute distribution in billet continuous casting process

TAO WANG[1,2,3], ENGANG WANG[1,3], YVES DELANNOY[4], YVES FAUTRELLE[2], and OLGA BUDENKOVA[2]

1) Key Laboratory of Electromagnetic Processing of Materials (Ministry of Education), Northeastern University, No. 3-11, Wenhua Road, Shenyang 110004, P. R. China.

2) Univ. Grenoble Alpes, CNRS, Grenoble INP, SIMAP, F-38000 Grenoble, France.

3) School of Metallurgy, Northeastern University, Shenyang 110004, P. R. China.

4) Univ. Grenoble Alpes, CNRS, Grenoble INP, LEGI, F-38000 Grenoble, France.

Author's email address:

TAO WANG: epm_wangtao@163.com

ENGANG WANG: egwang@mail.neu.edu.cn

YVES DELANNOY: yves.delannoy@grenoble-inp.fr

YVES FAUTRELLE: yves.Fautrelle@grenoble-inp.fr

OLGA BUDENKOVA: olga.budenkova@grenoble-inp.fr

Correspondent: egwang@mail.neu.edu.cn (ENGANG WANG)

ABSTRACT: A volume averaged columnar solidification model, which couples the flow, temperature and solute concentration fields, is applied to simulate experimental casting cases with and without vertical electromagnetic stirring (V-EMS). The calculated distribution of electromagnetic intensity and final macrosegregation maps are consistent with the experimental results. Calculation results reveal that the V-EMS promotes longitudinal melt flow, accelerates heat dissipation, shortens the solidification end and reduces the central segregation of carbon. However, when V-EMS is applied, the solute distribution becomes asymmetric because the melt flow shows opposite directions between the near and far sides from stirrer. An obvious positive segregation band is observed at about 1/4 width of the billet near the stirrer in both calculated and experimental results. The position and degree of such positive segregation could be affected by installation height of stirrer, as demonstrated by additional simulation cases.

KEY WORDS: vertical electromagnetic stirring; macrosegregation; volume averaged method; continuous casting

Declarations

Funding

The authors gratefully acknowledge financial support from the National Nature Science Foundation of China (Grant No. U1760206), the National Key R&D Program of China (Grant No. 2017YFE0107900), the 111 Project 2.0 of China, No. BP0719037). The SIMAP laboratory acknowledges the financial support provided by the ESA-MAP MICAST project contract 14347/01/NL/SH.

Availability of data and material

The datasets used or analysed during the current study are available from the corresponding author on reasonable request.

Code availability

Not applicable.

Author Contributions: Conceptualization

Conceptualization, E.W.; literature search, O.B. and T.W.; development of numerical code, T.W., O.B. and Y.D.; calculation and production of figures, T.W.; data analysis, E.W., Y.D., and O.B.; mathematical description, Y.F.; original draft preparation, T.W. All authors have read and agreed to the published version of the manuscript.

Ethics approval

Not applicable.

Consent to participate

Not applicable.

Consent for publication

Not applicable

Article Highlights

Predicted macrosegregation map of continuous casting billet correlates well with experimental results.

Vertical electromagnetic stirring promotes longitudinal melt flow and reduces central segregation.

Installation height of electromagnetic stirrer affects the shape of positive segregation band.

1 Introduction

Electromagnetic stirring (EMS) is often applied during solidification to homogenize the solidification structure and to limit the extent of macrosegregation and a proper application of EMS can help improving the quality of continuous cast product[1-4]. There exist various types of EMS, among which rotational electromagnetic stirring (R-EMS) and linear electromagnetic stirring (L-EMS) are most commonly applied in continuous casting processes. In general, R-EMS is used in round or bloom caster[5] while L-EMS is often used at wide face of slab caster[6]. A R-EMS always generates electromagnetic force which act in the plane perpendicular to the casting direction while for L-EMS, the direction of generated electromagnetic force depends on the arrangement of magnetic poles. Particularly, if the poles of L-EMS are arranged along casting direction, axially moving magnetic flux will be imposed on melt in or against the casting direction. Such type of EMS in vertical continuous casting is called V-EMS[7,8]. Depending on casting configuration, the fluid flow may strongly depend on the direction of the electromagnetic force, consequently, solidification process can be also affected in various ways[9]. In principle, the R-EMS generates peripheral flow in stirring region while the V-EMS generates longitudinal flow, and combination of R-EMS and L-EMS can produce spiral flow of melt[10-11]. Many theoretical and experimental investigations have been made regarding the effect of R-EMS or L-EMS in continuous casting process[6,12-15]. However, multiple industrial examples demonstrate that effect of the EMS depends on actual configuration of the casting process and that of the stirrer, as well as on the positioning of the latter[16,17]. In order to have an in-depth understanding of the mechanism how V-EMS affects solidification during continuous casting process, recently a series of experiments with casting of high carbon bearing steel were carried out by Xu et al.[7,8]. In those works, the effect of V-EMS on microstructure and macrosegregation of cast products has been presented in detail. However, due to constraints, usual for industrial process in harsh, in-situ observation was not realised, and only post-mortem analysis was made for samples from casts, which provides information only about the final state of solidification. Therefore, numerical simulation is indispensable for having clearer and comprehensive understanding on such topic.

Numerically, the effect of the EMS on the flow in bloom caster was analyzed by Dubke[17], but without considering the solidification. Barman et al.[15] simulated the solidification of aluminum alloy ingot under EMS by coupling the heat transfer, fluid flow, solute transport, and multiphase evolution. However, in that research, segregation of elements during solidification was estimated simply by Scheil equation. It can be assumed that a more detailed description of grain growth can provide more information regarding formation and development of macrosegregation. The up do date solution is to apply the volume averaged method, which introduces a representative elementary volume to embed the microscopic phenomena into a larger macroscopic system. Since first proposed by Rappaz et al.[18] and Beckermann et al.[19], this modeling method has been developed quickly during past decades[20]. Compared with continuum media model or porous media model, volume averaged model introduces the growth kinetics through its averaging process over microscale

structure and transport phenomena. Compared with cellular automaton method[21], phase field method[22] or recently proposed needle network model[23], volume averaged model demands less dense calculation mesh i.e. consumes less computational resources. Based on volume averaged method, simulations for ingot solidification have been carried out to investigate the mechanism of macrosegregation formation[24-25] and the effect of electromagnetic stirring[26]. Recently, such class of models were introduced to the computer simulation of continuous casting processes[27-29].

In the current work, the solidification process of casting experiment is simulated using a volume averaged solidification model. Simulation is conducted in the 2D vertical central symmetric plane of a small billet. The interaction between the fluid flow and the grain growth, as well as the formation of the macrosegregation are investigated in detail. The characteristic of V-EMS and its role in a casting process is revealed through the comparison between cases with and without V-EMS.

2 Experiment introduction

The continuous casting experiment to be simulated was made in EPM laboratory of Northeastern University[7,8]. The experimental system concerns apparatuses including mold, electromagnetic stirrer, water spraying system and dummy bar. Simulation is made in 2D in xy-plane, as schematically presented in Fig. 1.

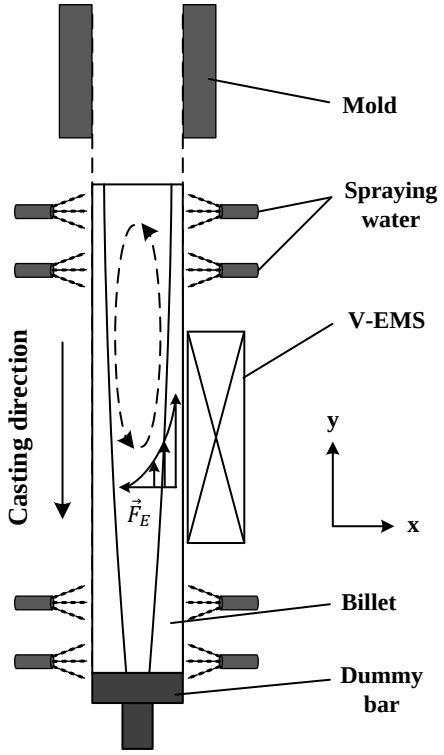

Fig. 1 Schematic representation of the continuous casting system

Before the continuous casting started, the weighted GCr15 (liquidus temperature: 1726 K) ingot was melted in an induction furnace and held with the overheat of 40 K for 2 hours. Then the molten

steel was poured into the mold and pulled down due to the displacement of the dummy bar with constant velocity of 0.6 m/min. The molten steel firstly formed a shell due to strong cooling in the mold, and then the shell with inside melt was cooled down from surface by spraying water during the following section with height of 1.25 m. An electromagnetic stirrer was set at 0.4 m below the end of mold, which generated the Lorentz force pointing upwards in billet in the spraying water cooling region. After that, the billet with length of about 0.6 m was pulled out of spraying water region and finished its solidification in air. Related experimental parameters are summarized in Table 1.

Table 1 Process parameters of continuous casting experiment

Parameters, units	Values
Cross sectional size, m	0.1×0.1
Mold cooling length, m	0.4
Spraying water cooling length, m	1.25
Cooling water flux, m^3/h	3.4
Cooling water temperature, K	300
Cast speed, m/min	0.6
Superheat, K	20
V-EMS electric current/frequency, A/Hz	250/12

3 Model description

3.1 Basic assumptions

A two-phase columnar solidification model was established coupling electromagnetism, fluid flow, heat and solute transport with the following assumptions:

(1) The two phases in the model are the liquid melt (l- phase) and the columnar dendrite trunks (s- phase) that gives for the corresponding fractions: $f_l + f_s = 1$. Solid phase always attaches to the boundary walls and grows from casting surface into the center of melt.

(2) Permeability of s- phase is calculated according to the Kozeny-Carman equation[30] that assumes solid phase as porous media.

(3) Considering that the carbon is the main concern element in high carbon steel solidification, the equilibrium solute concentration is calculated upon binary Fe-C phase diagram. Model neglects the segregation behaviors of Si, P, Mn which should be similar to that of solute element C according to Choudhary and Gauguly[31].

(4) The oscillation of mold and the nozzle structure are neglected. The hot metal was assumed to be poured into the mold slowly with a constant rate.

(5) Both liquid and solid phases have same mass density in conservation equations. For the buoyancy force calculation, Boussinesq equation[32] is used, i.e. the liquid density is linearly dependent on temperature and solute concentration.

3.2 Governing equations of solidification model

3.2.1 Mass transfer

The mass conservation equations for liquid and solid phases are expressed as follows:

$$\frac{\partial(f_l\rho_l)}{\partial t} + \nabla(f_l\rho_l\vec{u}_l) = -M_{ls} \qquad (1)$$

$$\frac{\partial(f_s\rho_s)}{\partial t} + \nabla(f_s\rho_s\vec{u}_s) = M_{ls} \qquad (2)$$

where $M_{ls} = f_l \cdot \rho_l \cdot S_i^M \cdot v_i$ is mass transfer rate from liquid phase to solid phase. The dendritic trunks are assumed as cylinders (Fig. 2) and the interface movement is driven by diffusion of the solute in the interdendritic liquid. Therefore, the surface area concentration S_i^M and the lateral growth velocity of the columnar trunks v_i can be obtained by[33]:

$$S_i^M = \frac{2d_c\pi}{\sqrt{3}\lambda_1^2} \qquad (3)$$

$$v_i = \frac{2D_l}{d_c} \cdot \frac{c_l^* - c_l}{c_l^* - c_s^*} \left[\ln\left(\frac{2\lambda_1}{\sqrt{3}d_c}\right)\right]^{-1} \qquad (4)$$

where $d_c = \lambda_1 \cdot \sqrt{\sqrt{12}f_s/\pi}$ is the diameter of columnar trunks; λ_1 is primary arm spacing, interface concentration is given according to thermodynamic equilibrium: $c_l^* = c_s^*/\mathrm{k} = (T_l - T_0)/m$, k is partition coefficient.

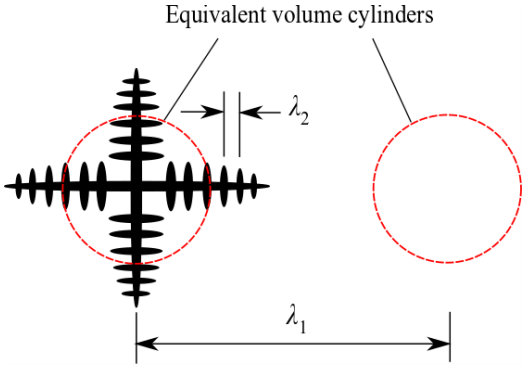

Fig. 2 Schematic of the cross-section of growing columnar trunks

3.2.2 Multiphase flow

Momentum conservation for liquid phase can be described through Navier-Stokes equation.

$$\frac{\partial(f_l\rho_l\vec{u}_l)}{\partial t}+\nabla(f_l\rho_l\vec{u}_l\vec{u}_l)=-f_l\nabla p+\nabla\left[(\mu_l+\mu_{t,m})f_l(\nabla\vec{u}_l+(\nabla\vec{u}_l)^{\mathrm{T}})\right] -\vec{u}_lM_{ls}+\vec{F}_{Bl}+\vec{U}_{sl}^{D}+f_l\vec{F}_E \quad (5)$$

where $\mu_{t,m}$ is turbulent viscosity calculated with a mixture realizable $k-\varepsilon$ turbulent model[34] Eqs. (6-7) give expressions for the thermo-solutal buoyancy force $\vec{F}_{Bl}$ as well as the drag force from solid dendrites $\vec{U}_{sl}^{D}$ that is calculated by Kozeny-Carman equation. The calculation for electromagnetic force $\vec{F}_E$ is detailed in section 3.3.

$$\vec{F}_{Bl}=f_l\rho_l\vec{g}\left[\beta_T\left(T_l^{ref}-T_l\right)+\beta_C\left(c_l^{ref}-c_l\right)\right] \quad (6)$$

$$\vec{U}_{ls}^{D}=\frac{20\pi^2\mu_lf_s^2}{f_l\lambda_2^2} \quad (7)$$

3.2.3 Solute transport

Average solute concentration for each phase can be calculated through the following equations:

$$\frac{\partial(f_l\rho_lc_l)}{\partial t}+\nabla(f_l\rho_l\vec{u}_lc_l)=\nabla(D_lf_l\nabla c_l)-kc_l^*M_{ls} \quad (8)$$

$$\frac{\partial(f_s\rho_sc_s)}{\partial t}+\nabla(f_s\rho_s\vec{u}_sc_s)=k\cdot c_l^*\cdot M_{ls} \quad (9)$$

where D_l is the diffusion coefficient and can be expressed as $D_l(T)=D_0\exp(-Q/(RT))$[12].

3.2.4 Enthalpy conservation

The energy conservation is treated in two-phase form, implying that the temperatures of solid and liquid phases are solved separately. They can be expressed with the following equations:

$$\frac{\partial(f_l\rho_lh_l)}{\partial t}+\nabla(f_l\rho_l\vec{u}_lh_l)=\nabla(k_lf_l\nabla T)+LM_{ls}f_l+H^*(T_s-T_l) \quad (10)$$

$$\frac{\partial(f_s\rho_sh_s)}{\partial t}+\nabla(f_s\rho_s\vec{u}_sh_s)=\nabla(k_sf_s\nabla T)+LM_{ls}f_s+H^*(T_l-T_s) \quad (11)$$

where $h_l=\int_{T_{ref}}^{T_l}c_p^ldT+h_l^{ref}$; $h_s=\int_{T_{ref}}^{T_s}c_p^sdT+h_s^{ref}$; $H^*=10^9\ \mathrm{W/(m^2K)}$ is an "infinite" volumetric heat exchange rate between two phases.

3.3 Electromagnetic force

Solution for the electromagnetic problem can be obtained for the system shown in Fig.3, where the electromagnetic field generated by the inductor penetrates the metallic region. For the subsequent equations the *y'*-direction points into the metallic medium with the origin *y'* = 0 at its surface. Based on Maxwell equations, the analytical solution for time averaged electromagnetic force $\vec{F}_E$ is given as[35]:

$$F_{Ex'} = \delta(x')\frac{\sigma\omega}{2k}\mathrm{B_0}^2 e^{-2y'\sqrt{\frac{k^2}{2}+\frac{1}{2}\sqrt{k^4+\sigma^2\mu^2\omega^2}}} \quad (12)$$

$$F_{Ey'} = \delta(x')\frac{\sigma\omega}{2k^2}\mathrm{B_0}^2\sqrt{-\frac{k^2}{2}+\frac{1}{2}\sqrt{k^4+\sigma^2\mu^2\omega^2}}\, e^{-2y'\sqrt{\frac{k^2}{2}+\frac{1}{2}\sqrt{k^4+\sigma^2\mu^2\omega^2}}} \quad (13)$$

where $i = \sqrt{-1}$ is imaginary unit; σ is electric conductivity; μ is magnetic permeability; $\omega = 2\pi f_0$ is the angular velocity of current; $k = \pi/\tau$ is the wave number and $\tau = 0.15$ m is the pole pitch; B_0 is the amplitude of $\vec{B}$ at $y' = 0$. $\delta(x')$ represents the distribution interval of electromagnetic field.

$$\delta(x') = \begin{cases} 1 & \text{if } x'_{\min} < x' < x'_{\max} \\ 0 & \text{else} \end{cases} \quad (14)$$

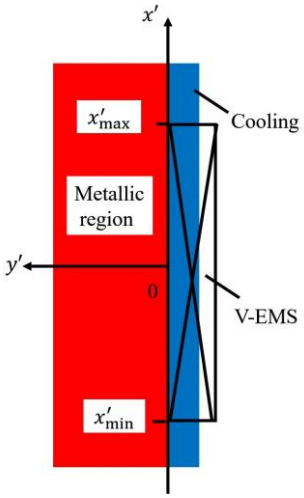

Fig. 3 Coordinate system for calculation of electromagnetic field

It should be noted that the expression of the electromagnetic forces neglected the presence of the mold wall and the end effects in the frame of a heuristic model. In order to verify the calculation results, distribution of magnetic induction intensity B_{eff} is compared with the values measured in space without the metal charge using Lake Shore-475 Gauss meter counter.

$$B_{eff} = \frac{B_0 e^{-ky'}}{\sqrt{2}} \quad (15)$$

As shown in Fig. 4(a), the calculated distribution of B_{eff} agrees well with measured values obtained under the offline state. Both calculation and measurements show that the magnetic induction intensity decreases exponentially from the surface to the geometry center of the setup. The maximum value of B_{eff} (0.32 kGs) appears at the place nearest to the V-EMS surface, then it decreases to 0.12 kGs at about 0.06 m from surface of V-EMS. Distribution of calculated electromagnetic force at different directions are presented in Fig. 4(b). Results show that the

electromagnetic force in *y*-direction is much smaller than that in *x*-direction, in other words, the EMS mainly acts along the vertical direction.

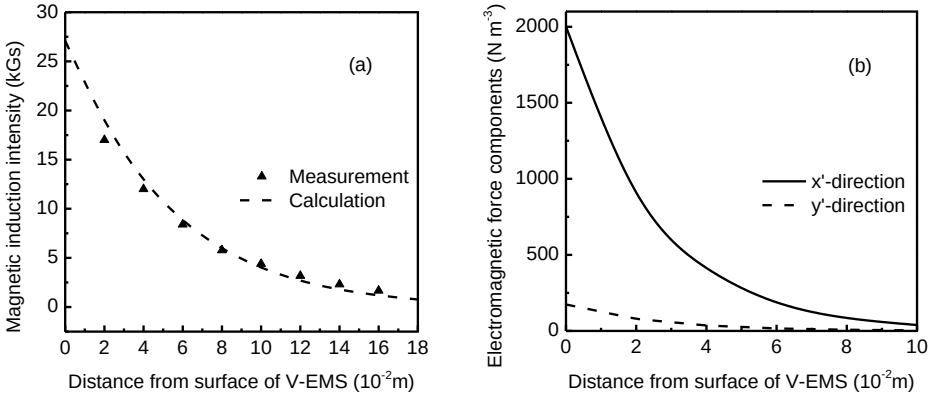

Fig. 4 Calculated and measured distribution of electromagnetic induction intensity (a) and calculated time averaged distribution of electromagnetic force components (b)

3.4 Boundary condition

During the solidification of continuous casting, the heat transfer process comprises of the mold cooling, secondary cooling and air cooling, all of which can be described by effective heat transfer coefficients. In copper mold cooling zone, the heat transfer rate from the billet is less intense at lower region because of the widening of air gap between mold and billet induced by solidification shrinkage. The heat transfer coefficient in the mold h_m is calculated according to Yamazaki et al.[36]

$$h_m = 1256\ e^{1.31z/(60v)}\ \mathrm{W/(m^2K)} \qquad (16)$$

where *z* is the distance from the top of the mold, and *v* is casting speed.

In the secondary cooling zone, the heat is extracted from the billet surface by spraying water. According to Nozaki et al.[37], the heat transfer coefficient h_w can be expressed as:

$$h_w = \frac{1570W^{0.55}(1-0.0075T_w)}{\beta}\ \mathrm{W/(m^2K)} \qquad (17)$$

where *W* is spraying water density, T_w is the cooling water temperature, and β is an empirical coefficient.

In the air cooling zone, the heat radiated from strand surface is calculated by the Stefan–Boltzmann law, correspondingly, the heat transfer coefficient h_{rad} is written as:

$$h_{rad} = \sigma\varepsilon\left(T_{surf}^2 + T_{amb}^2\right)\left(T_{surf} + T_{amb}\right)\ \mathrm{W/(m^2K)} \qquad (18)$$

where σ is Stefan–Boltzmann constant, ε is steel emissivity, T_{surf} and T_{amb} are the strand surface temperature and the ambient temperature respectively.

The whole model employs two different time steps. Microscale evolution, including the grain growth and solute transport between phases, is calculated with a smaller step size. Macroscale physical fields, like multiphase flow, transport of energy, solute and nuclei density, are solved by ANSYS FLUENT® software with a larger step size. The physical properties used in the numerical simulation are collected in Table 2.

Table 2. Material properties

Parameters	Value
Density，kg m^{-3}	7200
Electric conductivity，A V^{-1} m^{-1}	7.14×10^{5}
Latent heat, J kg^{-1}	2.72×10^{5}
Viscosity kg $m^{-1}s^{-1}$	0.006
Thermal conductivity of solid, W m^{-1} K^{-1}	26
Thermal conductivity of liquid, W m^{-1} K^{-1}	39
Specific heat，J Kg^{-1} K^{-1}	725
Emissivity	1
Primary arm spacing, μm	50
Secondary arm spacing, μm	20
magnetic permeability, V s A^{-1} m^{-1}	1.2566×10^{-6}

4 Results and discussion

Below, the simulations that are made for casting cases with and without EMS are presented in the section 4.1 and 4.2, respectively. Then, to demonstrate the effect of V-EMS on the solidification, a detailed comparison of the obtained results is presented in the section 4.3. In section 4.4 effect of the stirrer position and size on macrosegregation is considered through numerical simulations.

4.1 Solidification Process without V-EMS

During vertical continuous casting process, the billet experiences three distinguished cooling stages, which happen in mold, spraying water zone, and air cooling zone, respectively. The evolution of flow field, phase distribution and solute distribution are presented with snapshots at four representative times (45 s, 90 s, 135 s, 225 s). The schematic of the position of billet is provided in Fig. 5(a) where the dark blue color represents the strong cooling condition in the mold, the light blue color represents the water spray cooling zone, and the even lighter color represents the air cooling zone. Calculated results are presented in Fig. 5(b) with indication of time. Due to the symmetrical nature of the billet, only half of each physical field is given. The left half division is the solid phase fraction overlaid with liquid flow velocity vectors, while the right half shows the distribution of averaged mixture concentration: $c_{mix} = (f_l\rho_l c_l + f_s\rho_s c_s)/(f_l\rho_l + f_s\rho_s)$. It should be noted that the velocity vectors presented in Fig. 5(b) indicate the moving speed of the liquid phase relative to the solid shell, which continuously moves downwards under the pulling of the dummy bar.

An initial shell of small thickness quickly forms at the surface of strand in the mold own to the strong cooling condition. The molten steel near the solidified shell has a large temperature gradient pointing inwards. As the colder molten steel near the shell is heavier, it flows downwards to the bottom, resulting in an upward return flow at the melt center. At t = 45 s, the maximum velocity in liquid is about 6.16 mm/s and a front part of billet has been pulled out of mold and enters the spraying water cooling zone. The downward flow continuously transports the solute to the lower end region, therefore, an enriched layer appears near the bottom. At t = 90 s, the billet has entered into the water spray cooling zone and the shell thickness increases. Temperature gradient and the thermal buoyancy force in the melt decrease due to the decrease of the cooling intensity and also to the increase of the shell's heat resistance. Finally, the melt flow velocity is significantly reduced. At t = 135 s, the slab completely enters into the spray water cooling zone. The flow direction of molten steel near the shell gradually reverses from downward to upward because the melt at the solidification frontier is getting carbon enriched and becomes lighter. Due to the flow resistance in the mushy zone, the flow velocity of liquid is greatly reduced. At t = 225 s, the billet enters into air cooling region and the surface cooling intensity gets weaker. The solute element continues to be rejected by the growing solid phase and pushed by the solidification front into the liquid phase, eventually forming a strong central segregation.

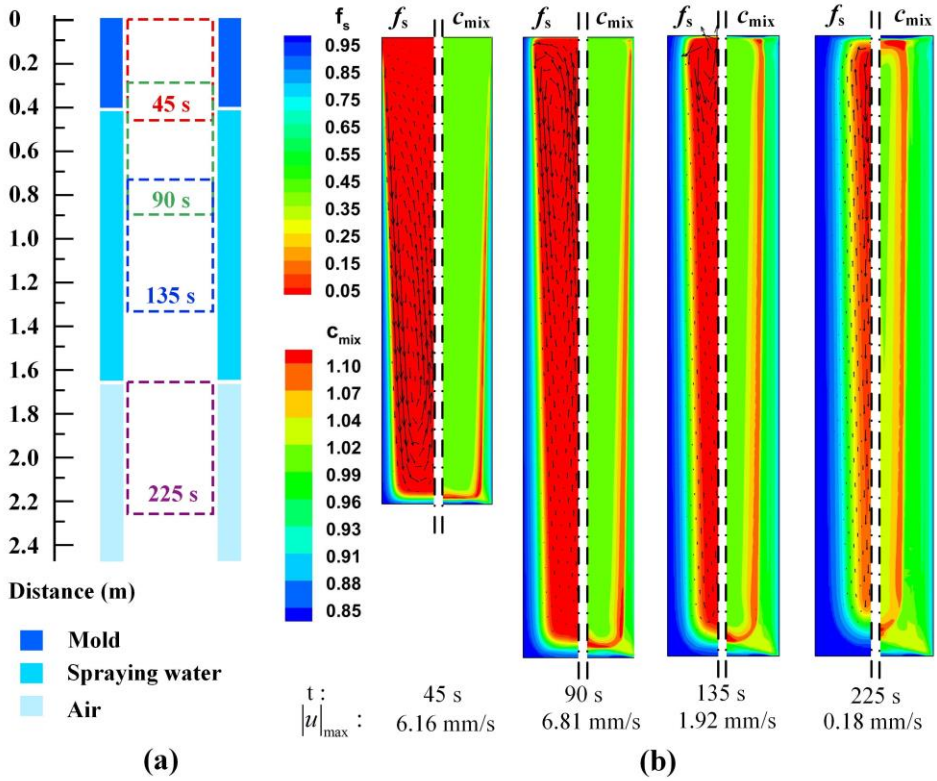

Fig. 5 Schematic position of billet at each solidification time (a), and flow field, solid phase fraction distribution and solute distribution at different solidification time of vertical continuous casting process without V-EMS (b)

4.2 Solidification Process with V-EMS

For the case with the application of V-EMS, the flow motion of melt is greatly changed. After initial solidification process up to t = 90 s, the billet arrives at the region where V-EMS can have effect on it. An upward electromagnetic force is stimulated in the melt near the stirrer by the travelling electromagnetic field. A counterclockwise vortex is formed at the stirring region and the flow velocity of the melt is significantly intensified. For the sake of concision, only the results at t = 135 s and t = 225 s are provided (Fig. 6(b)). Note that the symmetry of the process is destroyed due to the stirring. At t = 135 s, the melt near the stirrer flows upwards, driving the colder and more enriched melt at the bottom to an upper place. On the contrary, the hotter and fresher melt at the other side moves downwards, causing the horizontal asymmetric solute distribution. This flow results in a higher solute concentration near the stirrer side. The maximum velocity occurs at upper part of billet and it is around 15.1 mm/s. After the billet has left the stirring zone, such melt flow continues for a while and then gradually disappears. At t = 225 s, the melt flow becomes very weak with the maximum velocity of only 0.08 mm/s, which is due to the quick growth of solid phase.

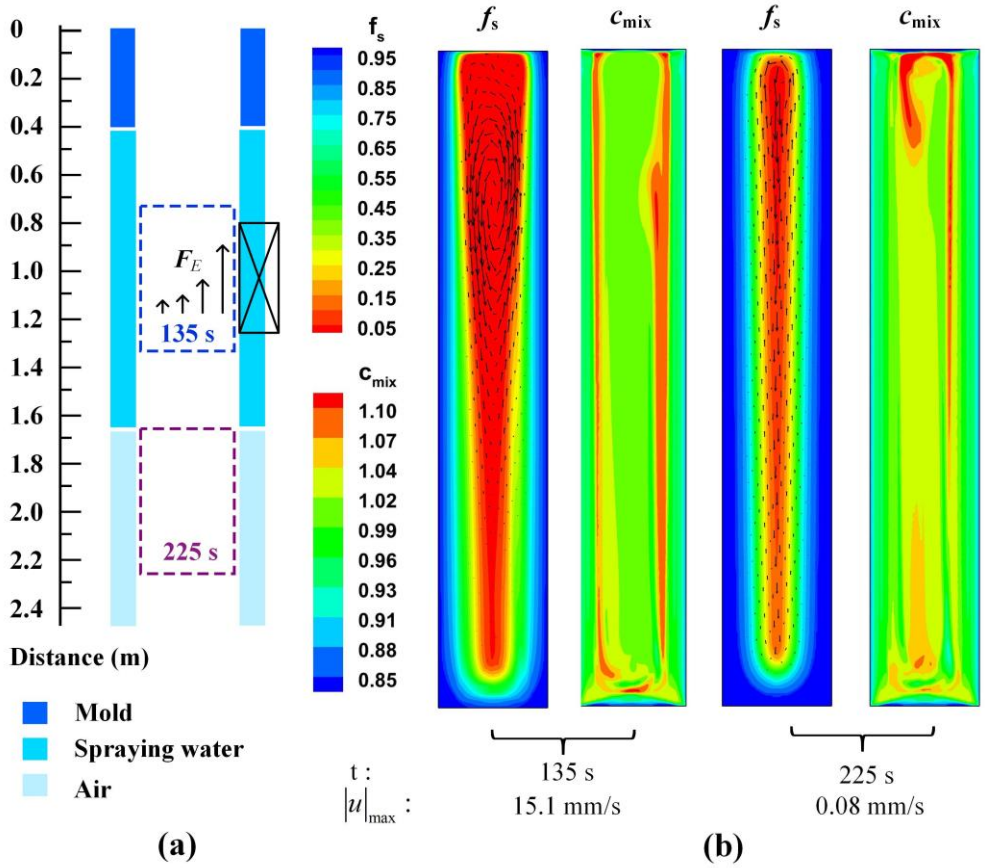

Fig. 6 Schematic position of billet at each solidification time (a), and flow field, solid phase fraction distribution and solute distribution at different solidification time of vertical continuous casting process with V-EMS (b)

4.3 Comparison of results between cases

4.3.1 Temperature and solid fraction

In order to further analyze the effect of the V-EMS, the evolution of profile of temperature and solid phase fraction along horizontal direction at middle height of billet are presented in Fig. 7. Comparison shows that the application of V-EMS increases the temperature of about 100 K at the surface of billet, which means the heat extraction from billet is promoted. Meanwhile, stirring slightly decreases the temperature at the center for about 5.5 K. Consequently, the difference of temperature between the surface and the center is diminished by V-EMS. According to Trindade et al.[14], smaller temperature gradient tends to promote the growth of equiaxed grains, which is beneficial to the final cast quality. It is found (Fig. 7(b)) that V-EMS promotes the solid growth in the billet, in particular, at t = 225 s, the solid fraction at the center of billet is 26% with use of V-EMS, while it is only 6.7% without EMS. V-EMS also enlarges the distance between the two solid fraction lines, indicating that the mushy zone is widen. Comparison between Fig. 5 and Fig. 6 shows that the length of liquid core is shortened, which is beneficial to the liquid feeding in billet and to reducing the shrinkage and porosity defects. An interesting observation is that the solid phase fraction profile has a obvious turning points at distance of 7.2 cm, which implies that the local solid growth rate is changed after the V-EMS is applied. Indeed, the stirring promotes the heat dissipation and solid growth, which will further affect the macrosegregation distribution as will be discussed below.

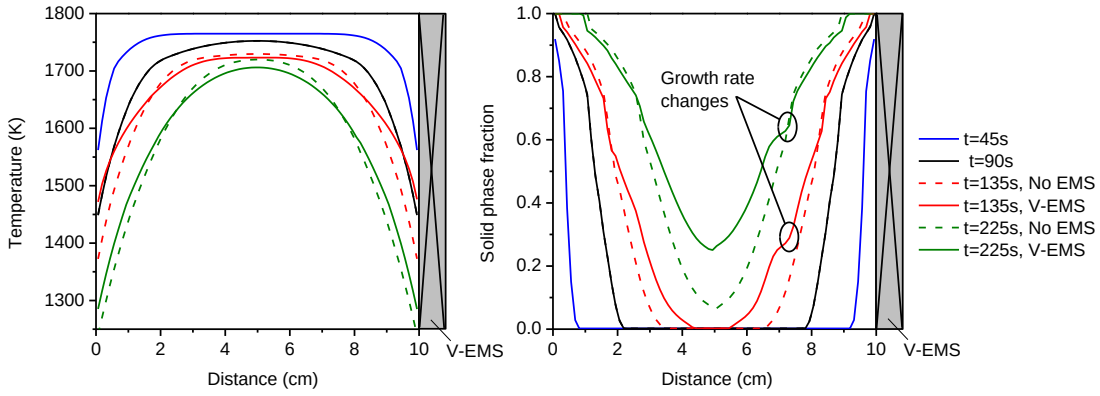

(a) (b)

Fig. 7 Distribution of temperature (a) and solid phase fraction (b) along cross section at middle height of billet with and without V-EMS

4.3.2 Macrosegregation Formation

Samples from longitudinal section of billet products were polished and etched to show their internal quality and macrosegregation either with or without V-EMS. As can be seen in Fig. 8, the slice sample with side length of 100 mm was etched with mixture liquid: $FeCl_3$, picric acid,

311 C_2H_5OH and H_2O. Obtained macrostructure of etched samples are shown in Fig. 9(a-b) with
312 calculated carbon segregation maps for the same region provided in Fig. 9(c-d).

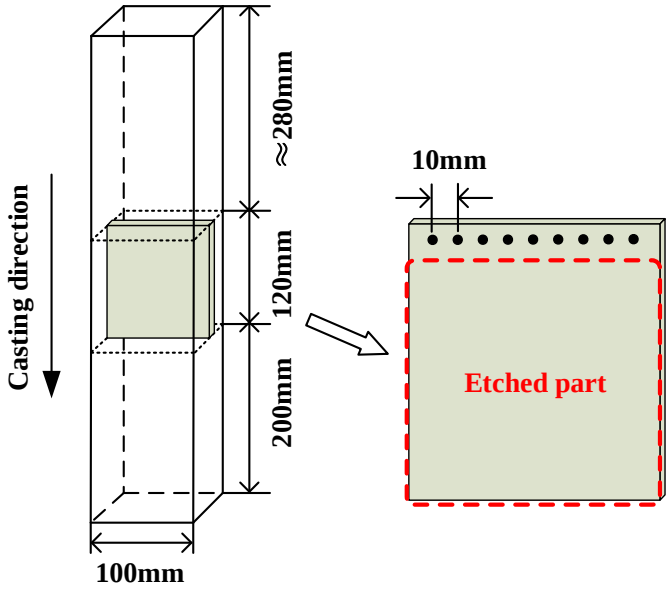

313

314 **Fig. 8** Sampling schematic diagram for the etching process and the carbon analysis

315

316 The morphology of etched samples and calculated macrosegregation maps are put together in
317 Fig. 9. Both experimental and calculated results show that the center segregation is decreased by
318 the V-EMS owing to the strengthened melt flow that accelerates the heat dissipation and solute
319 homogenization in the billet. Besides, the shrinkage and porosity defects are reduced or eliminated
320 because shortening of liquid core improves the feeding ability of liquid core. Another interesting
321 phenomenon is the positive segregation band appearing at the vicinity of the right 1/4 width region
322 (Fig. 9d) under the effect of V-EMS . On the one hand, the upward flow near the solidification
323 frontier brings up the enriched melt, increasing local solute concentration, on the other other hand,
324 electromagnetic stirring makes the melt near the right side solidify more quickly.

325 To have a more quantitative comparison for carbon segregation along the transverse direction,
326 different positions on the samples with an interval of 10 mm were drilled and chemically analyzed
327 by using Leco CS844 instrument. Measured carbon element at the points are plotted in Fig. 10,
328 where calculation results are added for comparison. The calculated central segregation is slightly
329 different from the experimental result. In experiment the center segregation ratio drops from 1.22 to
330 1.08 with the use of V-EMS while in simulation it drops from 1.16 to 1.12. According to the
331 experimental data, the segregation ratio in positive segregation band is nearly 1.11, while in
332 calculation, it is about 1.04. This difference can be attributed to the neglecting of shrinkage and
333 deformation of the solidified shell, which is believed to be important for the formation of central
334 segregation according to some other studies[28,38].

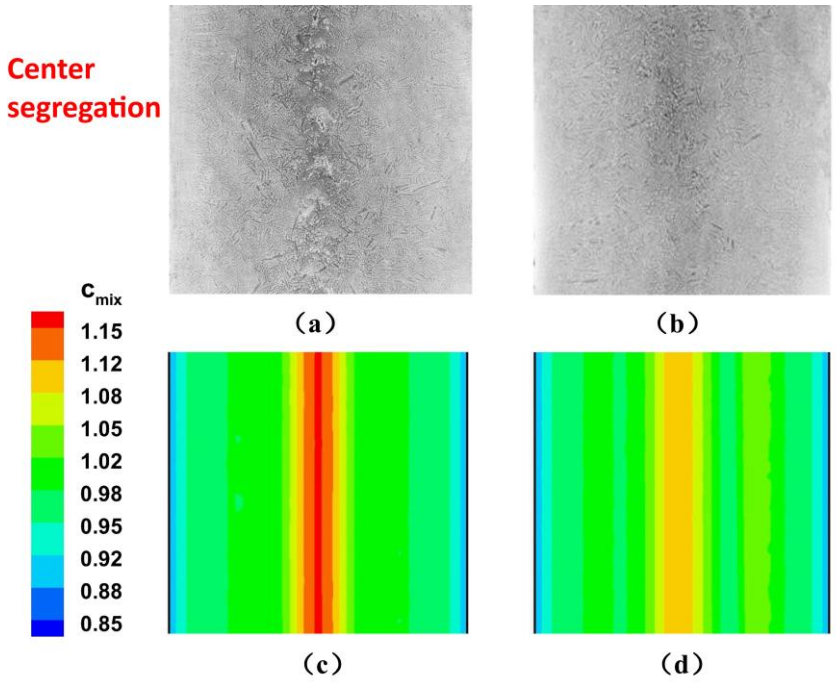

335

336 **Fig. 9** Morphology of a part of the vertical section of billets and calculated macrosegregation
337 distributions with (b, d) and without (a, c) V-EMS

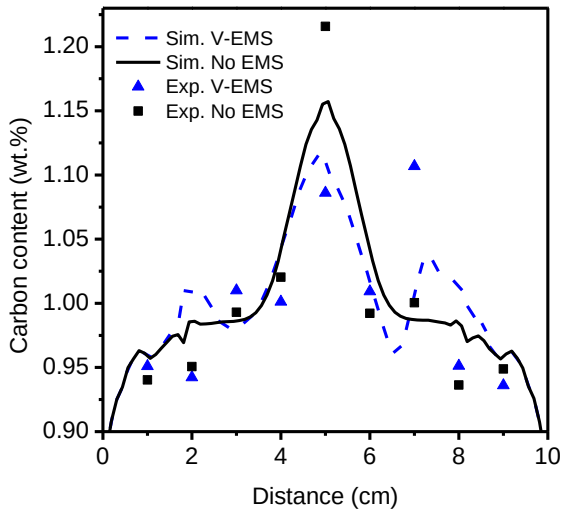

338

339 **Fig. 10** Comparison of the final macrosegregation distribution along along the transverse direction
340 between simulations and experimental measurements

341 **4.4 Effect of stirrer's installation height**

342 One of the imporant parameter for cast quality and energy consumption is the installation
343 height of the stirrer. In order to give some enlightenment to this problem, three additional
344 simulation cases were conducted, in which the positions of the stirrer moves from 0.8 m to 0.5 m,
345 1.1 m and 1.4 m below the meniscus, respectively. Casting speed, mold heat transfer coefficient and

material properties are kept same for all cases. Simulated fields of solid fraction, liquid flow and solute concentration under new positions of electromagnetic stirrer have been presented in Fig. 11. For the convenience of comparison, the results in Fig. 11 have same relative position between billet and stirrer as in Fig. 6. In each case, flow velocity of melt in lower part of billet is smaller because of larger solid phase fraction and larger flow resistance. It is also observed that the liquid pool width and melt flow velocity decreases with the position of stirrer displacing downwards.

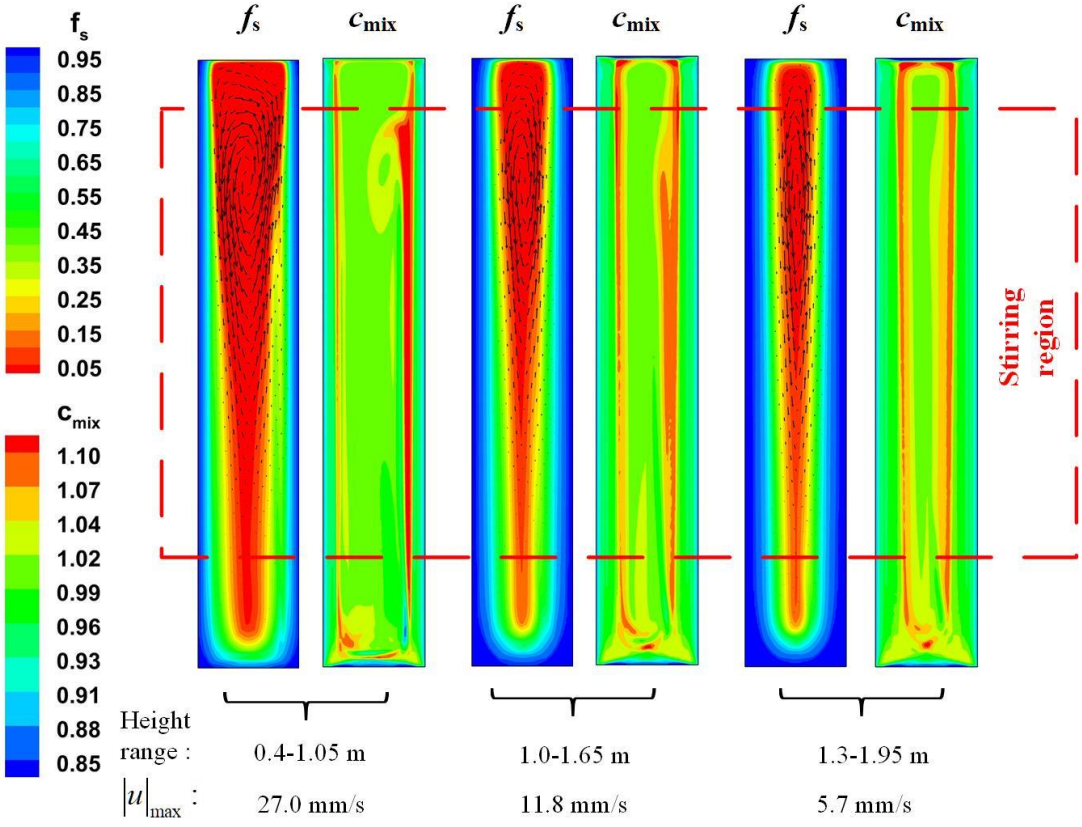

Fig. 11 Flow velocity vectors and solid fraction distribution at t = 135 s for the cases with different installation height of EMS

As illustrated in Fig. 12(a), when the installation height of EMS stirrer moves from 0.5 m to 1.4 m below meniscus, the maximum velocity drops from 2.7 cm/s to 0.6 cm/s, the position of maximal velocity displaced from 2.2 cm to 0.5 cm to the center of billet. The macrosegregation distribution is also greatly influenced by the installation height of EMS stirrer (Fig. 12(b)). When the V-EMS is installed at 0.5 m below meniscus, the carbon content shows large value in the position 2 cm away from surface, indicating a severe segregation band at this distance. When V-EMS is installed at lower position, i.e. closer to the solidification end, the segregation band becomes less intense, while the central segregation is not obviously changed.

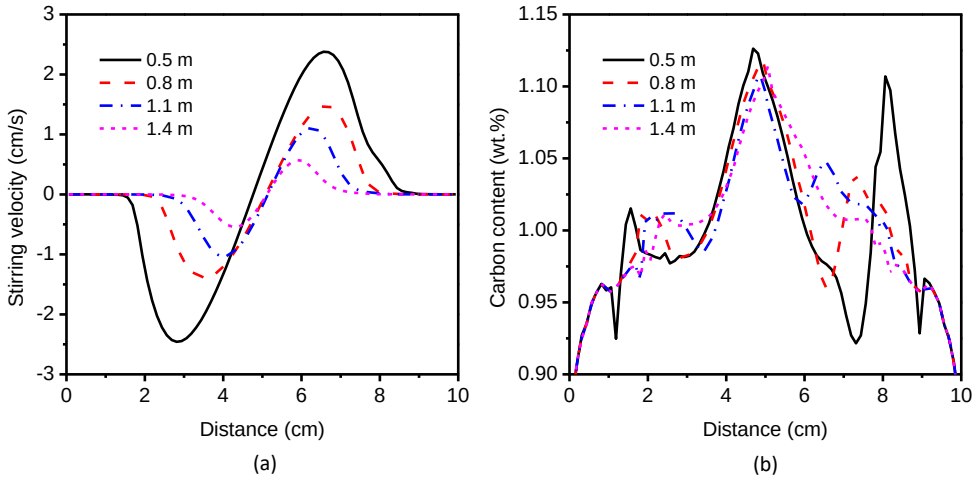

364

365 **Fig. 12** Comparison of liquid velocity profile(a) and macrosegregation profile(b) with different
366 installation height of EMS

367

368 **5 Conclusions**

369 In this paper, a volume averaged columnar model is used to simulate the solidification process
370 of GCr15 bearing steel continuous casting process. The evolutions of flow field, solid phase fraction
371 distribution and solute concentration distribution have been presented for cases with and without V-
372 EMS. Results show that V-EMS can promote the longitudinal melt flow, accelerate the superheat
373 dissipation and relieve central segregation. However, vertical stirring leads to opposite moving
374 directions of liquid between near and far sides from the stirrer, which causes positive segregation
375 band near the stirrer and horizontal solutal inhomogeneity. Lowering the installation position of V-
376 EMS helps relieving this kind of segregation band. In the future, more optimization has to be made
377 for the structure and application parameters of V-EMS.

378

References

1 K.S. Oh and Y.W. Chang, ISIJ Int. 35 (1995) 866–75.

2 S.M. Cho, B.G. Thomas, Metals (Basel) 9 (2019) 471.

3 F. Wang, E. Wang, L. Zhang, P. Jia, T. Wang, J. Manuf. Process. 26 (2017) 364–371.

4 D.B. Spencer, R. Mehrabian, M.C. Flemings, Metall. Mater. Trans. B 3 (1972) 1925–1932.

5 Y. Xu, X. J. Xu, Z. Li, T. Wang, A.Y. Deng, E. Wang, High Temp. Mater. Process. 36 (2017) 339–346.

6 D. Jiang, M. Zhu, L. Zhang, Metals (Basel) 9 (2019) 452.

7 Y. Xu, E.G. Wang, Z. Li, A.Y. Deng, J. Iron Steel Res. Int. 24 (2017) 483–489.

8 Y. Xu, T. Wang, F. Wang, E.G. Wang, J. Cryst. Growth 468 (2017) 506–509.

9 L. Hachani, K. Zaidat, Y. Fautrelle, Int. J. Heat Mass Transf. 85 (2015) 438–454.

10 W. Yang, X.D. Wang, B. Wang, F. Baltaretu, J. Etay, Y. Fautrelle, Metall. Mater. Trans. B 47 (2016) 2771-2784.

12 H. Sun, J. Zhang, Metall. Mater. Trans. B 45 (2014) 1133–1149.

13 O. Budenkova, A. Noeppel, J. Kovács, A. Rónaföldi, A. Roósz, A.M. Bianchi, F. Baltaretu, M. Medina, Y. Fautrelle, Mater. Sci. Forum, 649 (2010) 269–274.

14 L.B. Trindade, J.E.A. Nadalon, A.C.Contini, R.C. Barroso, Steel Res. Int. 88 (2017) 1–8.

15 N. Barman, P. Kumar, P. Dutta, J. Mater. Process. Technol. 209 (2009) 5912–5923.

16 N. Genma, T. Soejima, T. Saito, M. Kimura, Y. Kaihara, H. Fukumoto, K. Ayata, ISIJ Int. 29 (1989) 1056–1062.

17 M. Dubke, K.H. Tacke, K.H. Spitzer, K. Schwerdtfeger, Metall. Trans. B 19 (1988) 595–602.

18 M. Rappaz, P. Thévoz: Acta Metall. 35 (1987) 1487–97.

19 J. Ni, C. Beckermann, J. Mater. Process. Manuf. Sci. 2 (1993) 217–31.

20 M. Wu, A. Ludwig, A. Kharicha, Metals (Basel) 9 (2019) 229.

21 T. Carozzani, C.A. Gandin, H. Digonnet, M. Bellet, K. Zaidat, Y. Fautrelle, Metall. Mater. Trans. A 44 (2013) 873–887.

22 X. Tong, C. Beckermann, A. Karma, Model. Cast. Welding, Adv. Solidif. Process. VIII, New York.

23 D. Tourret, A. Karma, Acta Mater. 120 (2016) 240–254.

24 T. Wang, E. Wang, Y. Delannoy, Y. Fautrelle, O. Budenkova, Metals (Basel), 11 (2021) 262.

25 W. Tu, H. Shen, B. Liu, ISIJ Int. 54 (2014) 351–355.

26 T. Wang, L. Hachani, Y. Fautrelle, Y. Delannoy, E. Wang, X.D. Wang, O. Budenkova, Int. J. Heat Mass Transf. 151 (2020) 119414.

27 D. Jiang, M. Zhu, Metall. Mater. Trans. B 48 (2017) 444–455.

28 A. Pakanati, K.O. Tveito, M. M'Hamdi, H. Combeau, M. Založnik, Metall. Mater. Trans. A 50 (2019) 1773–1786.

29 Y. Zheng, M. Wu, A. Kharicha, A. Ludwig, IOP Conf. Ser. Mater. Sci. Eng. 143 (2016) 012032.

30 B. Wang, X.D. Wang, Y. Fautrelle, Metall. Mater. Trans. B 47 (2016) 3476-3488.

31 S.K. Choudhary, S. Ganguly, ISIJ Int. 47 (2007) 1759–1766.

32 M. Založnik, A. Kumar, H. Combeau, Comput. Mater. Sci. 48 (2010) 11–21.

33 J. Li, M. Wu, J. Hao, A. Ludwig, Comput. Mater. Sci. 55 (2012) 407–418.

34 T.H. Shih, W.W. Liou, A. Shabbir, Z. Yang, J. Zhu, Comput. Fluids 24 (1995) 227–238.

35 M. Dubke, K.H. Tacke, K.H. Spitzer, K. Schwerdtfeger, Metall. Trans. B, 19 (1988) 581–593.

36 M. Yamazaki, Y. Natsume, H. Harada, K. Ohsasa, ISIJ Int. 46 (2006) 903-908.

37 T. Nozaki, J. Matsuno, K. Murata, H. Ooi, M. Kodama, Tetsu-to-Hagané 62 (1976) 1503–1512.

38 R. Guan, C. Ji, C. Wu, M. Zhu, Int. J. Heat Mass Transf. 141 (2019) 503–516.